CHEMISTRY OF MATERIALS

Open Access



pubs.acs.org/cm

Article

# Tetrahedral vs Spherical Nanocrystals: Does the Shape Really Matter?

Marco Califano*

Cite This: *Chem. Mater.* 2024, 36, 1162−1171

Read Online

ACCESS | Metrics & More | Article Recommendations | Supporting Information

**ABSTRACT:** Tetrahedral nanocrystals (NCs) have emerged as promising structures whose shape can prove advantageous over the more conventional spherical structure, notably in the superior stability it affords in the growth of III−V nanostructures. However, it is still not clear in what other properties they differ from their spherical counterparts. It has been shown experimentally that the position of the first exciton peak in some materials is very different between spherical and tetrahedral dots of the same size. In spite of this evidence, however, in the absence of accurate theoretical sizing curves obtained specifically for tetrahedra, their size is, nevertheless, often estimated based on emission curves relative to spherical dots instead. Here, we provide a comprehensive theoretical characterization of tetrahedral nanocrystals made of technologically relevant Cd-based and In-based materials, including much needed bespoke calibration curves, band edge positions, and the size dependence of radiative recombination times, for side lengths ranging from ∼3 to over 8 nm, corresponding to structures containing from about 300 to over 3300 atoms. We also present a side-by-side comparison with the properties of nominally spherical NCs made of the same materials, as a function of both volume and confinement size, highlighting differences and similarities between the two types of structures, which are analyzed in terms of shape, degree of confinement, and number of facets. Our results will contribute to a better understanding of the properties of these versatile shapes and, by clarifying the differences with those of spherical nanostructures, enable a clear identification of the respective ideal application range for an effective and more tailored device exploitation.

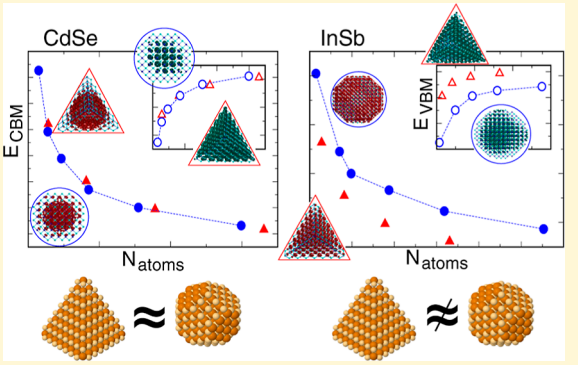




## INTRODUCTION

40 years ago, Brus' group published the first 'observation of [quantum] size effects in the electronic properties of small, crystalline CdS particles' in aqueous solution,[1] laying the foundations of modern nanotechnology. Since then, thanks to their size-, shape-, and composition-dependent electronic and optical properties, semiconductor nanocrystals (NCs) have become versatile building blocks for a variety of applications[2,3] evolving from a theoretical oddity to a multibillion dollar business.[4] Continuing advances in colloidal synthesis have, furthermore, made possible the growth of a wealth of different NC shapes, ranging from the original spherical-like nanoparticles, to more exotic and complex structures such as tetrapods,[5] octapods,[6,7] and hyperbranched NCs with rich 3D structures,[8] which have contributed to widen the application of these NCs. Recently, tetrahedrally shaped NCs have become increasingly popular, both as intermediates[9] (or end products[10]) in the synthesis of branched nanostructures and as individual entities in their own right.[11−15] These NCs are particularly interesting as their peculiar shape results[10,16] from the formation of (111)-equivalent cation-rich facets. In the case of InP,[16] these facets could be completely passivated with a combination of halides and primary amines, providing a general strategy for the growth of III−V NCs with controlled surfaces and superior stability.

The question therefore arises as to whether the electronic and optical properties of tetrahedral NCs differ from those of their spherical counterparts and, if so, whether their shape can lead to an increased functionality and new applications.

That this may indeed be the case was recently shown by Zhao et al.[17] who, exploiting the large contact area achievable between neighboring tetrahedra in thin-film assemblies, coupled with an effective surface passivation, obtained mobilities of the order of 0.45 $cm^2 V^{-1} s^{-1}$ in InP tetrahedral NCs (TNCs) with 8 nm edge length. This represents a huge improvement compared to the highest mobility reported[18] for spherical InP NCs (<0.1 $cm^2 V^{-1} s^{-1}$). Zhao et al.[17] and Kim et al.[16] further showed that also the optical properties, and, in particular, the position of the first exciton peak, of InP TNCs are very different from those of

Received: June 30, 2023
Revised: January 8, 2024
Accepted: January 8, 2024
Published: January 22, 2024

spherical NCs (SNCs) with the same size (where the size is the edge length $L$ in the former and the diameter $d$ in the latter). The lack of available sizing curves providing accurate gap versus size relationships derived specifically for tetrahedral structures is nevertheless forcing researchers to use inadequate calibration curves derived for spherical NCs[19] instead.

The reduced number of facets in tetrahedral NCs, although enabling complete passivation, could, however, be detrimental to their application in optically pumped NC lasers when compared to their spherical counterparts. Indeed, in a recent study on $CsPbBr_3$ NCs with different shapes but same average edge length and nearly identical absorption onset position,[20] the observed 2-fold increase in Auger recombination (AR) rates and 5.5-fold increase in the gain threshold for amplified spontaneous emission were associated with a reduction in the number of their facets (from 26, in rhombicuboctahedra, to 6, in cubes). These effects were, however, tentatively attributed[20] to the volume dependence of the Auger recombination constant[21] and explained as deriving from the volume decrease from rhombicuboctahedral ($V_{rh} = 2/3a^3(6 + 5\sqrt{2})$) to cubic ($V_c = a^3$) NCs with edge length $a$. If this were the case, however, as the ratio between the volumes of these structures is $V_{rh}/V_c = 8.7$, so should be the ratio between their Auger recombination times $\tau^{AR}$. The observed ratio was instead much lower than 8.7: $\tau^{AR}_{rh}/\tau^{AR}_{c} = 1.875$.[20] On the other hand, considering that the absorption onset is dictated by quantum confinement, which, in nanostructures, is usually determined by the shortest dimension (and not by the edge length), it is surprising that two shapes with octahedral symmetry (Oh) can exhibit the same absorption onset (to within 3 meV[20]), despite having volumes that differ by nearly 1 order of magnitude.

These inconsistencies raise the question of whether the Auger suppression observed in $CsPbBr_3$ NCs with different shapes may indeed have originated from an increase in the number of their facets. This would open the way to a new strategy to design Auger recombination rates based on shape engineering.

To address all these issues, we carried out a theoretical characterization of tetrahedrally shaped NCs of different sizes and different compositions, including most technologically relevant II−VI (Cd-based) and III−V (In-based) materials. Using a state-of-the-art atomistic semiempirical pseudopotential method[22] (SEPM), we compared their properties side by side with those of nominally spherical (but actually closer to truncated octahedral) NCs with similar sizes, volumes, and single-particle gaps (i.e., degree of confinement). We present accurate calibration curves (i.e., plots of the first exciton peak position vs size) and band edge positions for TNCs made of CdSe, CdTe, InP, InAs, and InSb, with side lengths ranging from $L \sim 2$ to $L \sim 8$ nm, including experimental data, where available, for comparison and validation.

## THEORETICAL METHOD

The NCs modeled in this work have a tetrahedral shape with four cation-rich (111)-equivalent facets[10,15,16] and a bulk-like crystal structure[14] (see Figure 1). This allowed us to accurately reproduce experimental samples. All NCs considered here (i.e., both tetrahedral and spherical) are modeled in their zincblende phase. The spherical dots have a cation-rich surface to enable a fairer comparison with the properties of their tetrahedral counterparts as the surface composition has been found in the past[23,24] to affect the optical properties of NCs made of different materials. The unsaturated bonds at the NC surface are

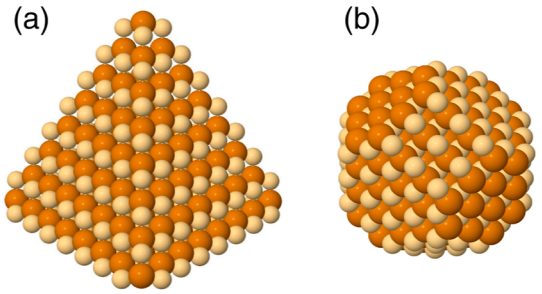


**Figure 1.** Nanostructures modeled in this work: tetrahedral NCs (front view, a) have four cation-terminated (111)-equivalent facets, whereas the nominally spherical NCs (b) have a truncated octahedral shape. Both have a bulk-like zinc-blende crystal structure. Yellow and orange spheres represent cations and anions, respectively.

passivated by pseudohydrogenic, short-range potentials with Gaussian form.[25] This procedure ensures ideal passivation, allowing us to focus on the intrinsic properties of these nanostructures. The single-particle energies $\varepsilon_i$ and wave functions $\psi_i$ are obtained by solving the Schrödinger equation using the plane-wave semiempirical pseudopotential method (SEPM),[22] including spin−orbit coupling. Excitonic effects are accounted for via a configuration interaction (CI) scheme, including Coulomb and exchange interactions,[26] where the excitonic wave functions $\Psi^{(i)}$ are expanded in terms of single-substitution Slater determinants $\Phi_{h,e}$ constructed using the single-particle wave functions as

$$\Psi^{(i)} = \sum_{h,e} C^{(i)}_{h,e}\Phi_{h,e} \tag{1}$$

Up to 20 valence states and 5 conduction states are used in this expansion, corresponding to CI basis sets of 400 configurations.

The k-space decomposition of the conduction band minimum (CBM) wave functions is performed following the procedure described in ref 23, where the high symmetry points $\Gamma$, $L$, and $X$ are used as seeds for a Voronoi partition of the Brillouin zone,[27,28] having the property that each wave vector contained in that partition (Voronoi cell) is closer to the specific high-symmetry point than to any other.

This well-benchmarked and accurate method has been used in the past to successfully predict a wide range of experimental features, including the size-dependent conduction and valence band edge energies in spherical NCs of different materials,[29] the exciton dynamics in CdTe[30] and InSb[23] colloidal dots, Auger rates in CdSe NCs,[31] and the electronic state properties of CdSe,[32] CdTe,[33] and CdTe/CdSe[34] tetrapods.

The room temperature lifetimes are calculated as

$$\frac{1}{\tau_R(T)} = \frac{\sum_i (1/\tau_i)e^{-\Delta E_i/k_BT}}{\sum_i e^{-\Delta E_i/k_BT}} \tag{2}$$

where we assume Boltzmann occupation of high-energy excitonic levels. $\tau_i$ is the radiative lifetime for the transition from state $\Psi^{(i)}$ to the ground state, obtained as[35]

$$\frac{1}{\tau_i} = \frac{4nF^2\alpha\omega_i^3}{3c^2}|M_i|^2 \tag{3}$$

where $n$ is the refractive index of the medium surrounding the NC (here, unless otherwise stated, we assume $n = 1.496$ corresponding to toluene), $F = 3\epsilon/(\epsilon_{dot} + 2\epsilon)$ is the screening factor, $\epsilon = n^2$, $\epsilon_{dot}$ is the size-dependent dielectric constant of the


https://doi.org/10.1021/acs.chemmater.3c01643
Chem. Mater. 2024, 36, 1162−1171

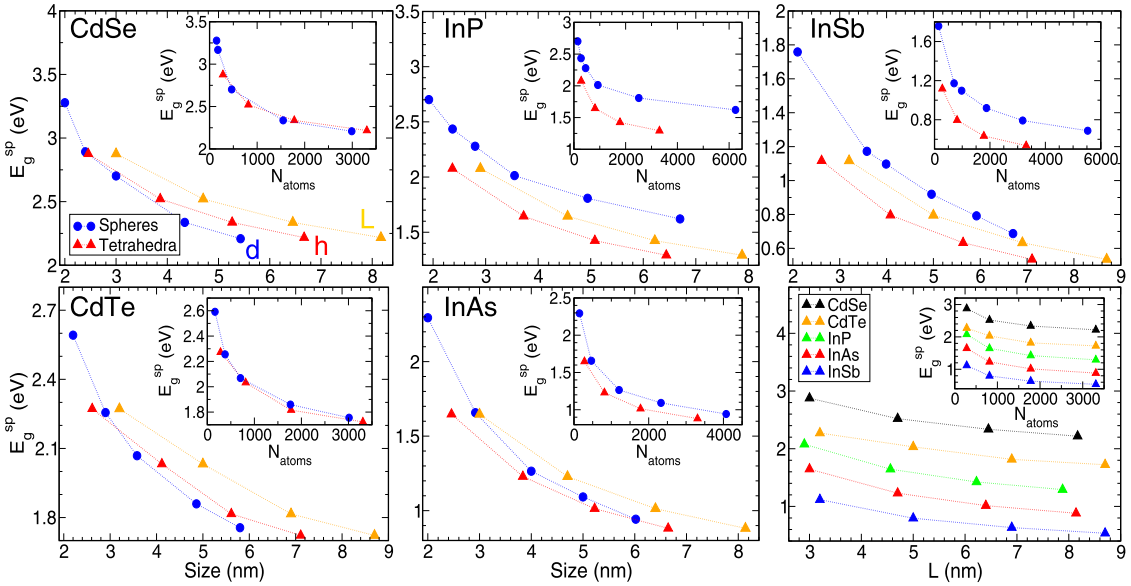


**Figure 2.** Single-particle energy gap vs size—sphere diameter $d$ (blue circles), tetrahedron height $h$ (red triangles), and side length $L$ (orange triangles)—(main panels), and vs volume (expressed as the total number of atoms $N_{atoms}$—insets), calculated for tetrahedral (triangles) and spherical (circles) NCs of different II–VI and III–V materials. The dotted lines are guides to the eye.

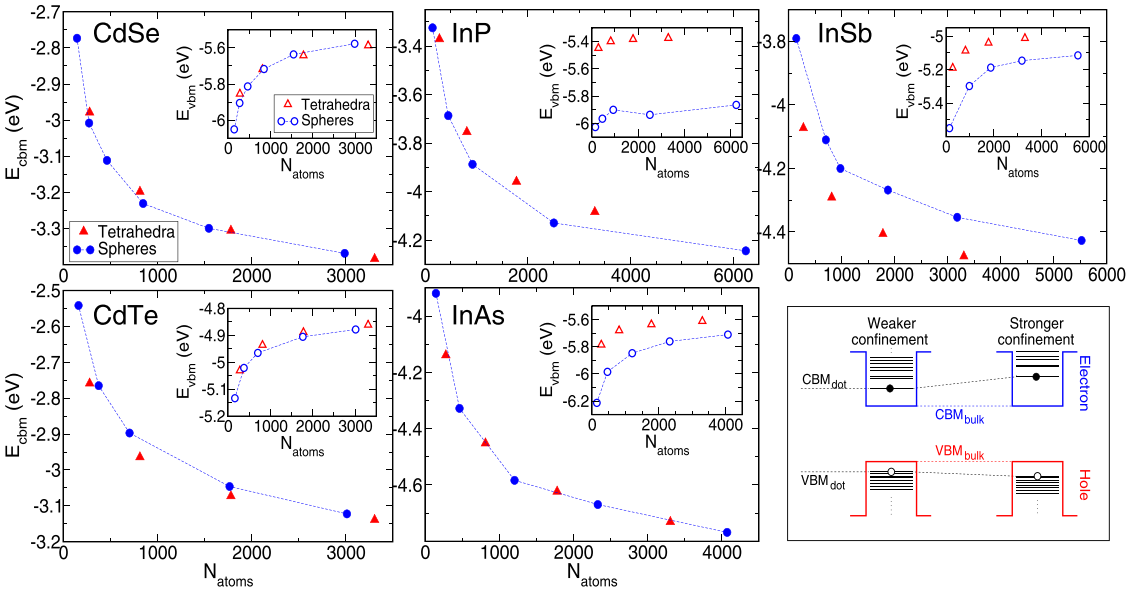


**Figure 3.** Conduction (main panels) and valence (insets) band edge energies vs volume (expressed as the total number of atoms $N_{atoms}$), calculated for tetrahedral (triangles) and spherical (circles) NCs of different II–VI and III–V materials. The dotted lines are a guide to the eye. The cartoon illustrates the effect of increasing the confinement on the position of the band edges.

quantum dot,[26] $\alpha$ is the fine structure constant, $\omega_i$ is the frequency of the emitted photon, $c$ is the speed of light, and

$$|M_i| = \sum_{h,e} C_{h,e}^{(i)} \langle \psi_h | \vec{r} | \psi_e \rangle \tag{4}$$

is the CI dipole moment.[26]

Auger recombination rates $W_i$ are calculated according to a consolidated procedure[31,36] as

$$W_i = \frac{\Gamma}{\hbar} \sum_n \frac{|\langle i|\Delta H|f_n\rangle|^2}{(E_{f_n} - E_i)^2 + (\Gamma/2)^2} \tag{5}$$

where $|i\rangle$ and $|f_n\rangle$ are the initial and final Auger states, $E_i$ and $E_{f_n}$ are their corresponding energies, $\Delta H$ is the Coulomb interaction, and the sum is over multiple final states $n$ (including spin), assumed to have a finite lifetime $\hbar/\Gamma$ (here $\Gamma$ = 10 meV is used). The Coulomb interaction $\Delta H$ is screened assuming a bulk-like dielectric within the NC ($\epsilon_{in} = \epsilon_{bulk}$) and the solvent dielectric constant outside it ($\epsilon_{out} = \epsilon_{solvent}$), the two regions connected by a function varying smoothly from $\epsilon_{in}$ to $\epsilon_{out}$ across the NC surface.[31,36]

## RESULTS AND DISCUSSION

According to recent effective-mass (EMA) calculations,[37] confinement is expected[16,37] to be stronger in tetrahedral nanostructures than in spherical ones with the same volume. We test this prediction by plotting in Figure 2 the single-particle energy gap $E_g^{sp} = E_{CBM} - E_{VBM}$ as a function of both NC size (i.e.,


https://doi.org/10.1021/acs.chemmater.3c01643
Chem. Mater. 2024, 36, 1162–1171

sphere diameter $d$ or tetrahedron height $h$ and side length $L$, main panels) and the total number of atoms $N_{atoms}$ (insets)[38] and in Figure 3, the conduction and valence band edge positions ($E_{CBM}$, main panels; $E_{VBM}$, insets) as a function of $N_{atoms}$ (in Figure S1, Supporting Information, we also provide the band edges positions as a function of size—sphere diameter and both side length and height for the tetrahedron—as this representation may be more relevant to experimentalists). While Figure 2 provides a measure of the *exciton* confinement, Figure 3 evidences the contribution of each individual charge carrier separately and isolates the degree of confinement of electron and hole wave functions in the two structures. It is clear that a simple effective-mass, particle-in-a-box (with an infinite confining potential) approach[37] is inadequate to capture the complexity of realistic nanostructures, where we find the confinement strength to depend more on the material than on the NC shape.

In Cd-based NCs, for example, the magnitude of the single-particle gap as a function of volume is very similar for both shapes (nearly identical in both CdSe nanostructures and slightly smaller in tetrahedral than in spherical CdTe NCs), following a similar behavior of the band edge positions in these two materials (nearly identical in spherical and tetrahedral NCs in CdSe structures; slightly closer to the bulk band edges, i.e., more weakly confined, in CdTe tetrahedral than in spherical CdTe NCs). The picture is more complex instead in In-based dots. Spherical NCs made of these materials exhibit a larger value of $E_g^{sp}$ suggesting that a stronger exciton confinement takes place in these shapes. We find that this is the result of a stronger confinement for the hole in all materials (the opposite of what is predicted by effective-mass calculations), despite (i) a more weakly confined electron in spherical than in tetrahedral structures in InP and (ii) the electron exhibiting nearly identical confinement in InAs NCs of both shapes.

Finally, in InSb, both charge carriers are more strongly confined in spherical structures than in tetrahedra, in striking contrast with the predictions of the particle-in-a-box calculations. This is not surprising, considering that even the more sophisticated **k·p** approach has been shown[39] to overestimate both electron and hole confinement energies in NCs made of both ionic and covalent materials owing to its failure to consider the coupling between conduction and valence bands, which is instead properly accounted for in our methodology.[39] Interestingly, however, we find that, in contrast with the conclusions of Fu et al.,[39] in this case, the effective-mass predictions are *less* accurate for materials with *larger* spin−orbit (SO) splittings (InSb and CdTe), in which Figure 3 shows the electron confinement to be clearly weaker in tetrahedra than in spheres with the same volume. In CdSe and InAs, where the SO splitting is similar (and about half of that in CdTe and InSb), the electron experiences virtually the same confinement in both shapes. Finally, in InP, whose SO splitting is about a quarter of that in CdSe, the electron confinement is stronger in tetrahedra, as predicted by EMA calculations. It is also interesting to note that this effect seems to correlate with the position the different anions occupy in the periodic table (and their electronic configuration), where P sits higher (and has no d electrons in its atomic orbitals), whereas As and Se are just below P (and have 3d electrons), and Sb and Te are located below As and Se (and have both 3d and 4d electrons). In this case, EMA predictions seem to be more accurate for lighter anions with simpler electronic structures.

The confinement strength in the different shapes is closely related to the degree of k-space mixing in the electron wave function.[40] This effect is quantified in Figure S2 (Supporting Information), in terms of the CBM contribution from different $k$ points in the Brillouin zone (we compare selected pairs of spherical and tetrahedral NCs with similar numbers of constituent atoms[41] made of different materials, representative of the three different situations occurring in Figure 3: electron confinement is stronger in either shape and similar in both shapes). Figure S2 (Supporting Information) shows that stronger mixing from $k$-points away from Γ (i.e., a smaller Γ component, with sizable contributions from the $L$ and $X$ points in the Brillouin zone), corresponding to a larger spread of the wave function in k-space, results in stronger electron confinement in real space. This is the case for InSb and InP, where, in the former, the larger mixing found in the SNC CBM wave function leads to more strongly confined electrons in spheres, whereas the opposite is true for InP (the larger mixing is exhibited by the TNC, leading to stronger electron confinement there). In contrast, in CdTe, where the contribution from off-Γ points is negligible for both shapes, the electron confinement is similar in both.

In the case of the VBM (Figure 3, insets), instead, the difference between the confinement in the two shapes (with the same volume) increases with increasing effective mass, from CdSe (where the hole experiences a similar degree of confinement in both tetrahedra and spheres) to InP (where the hole confinement energy in the two nanostructures can differ by over 0.5 eV). However, unlike in the case of the electron discussed above, in the latter material, we find that the k-space composition of the VBM is nearly the same in both shapes, and cannot, therefore, explain such a large difference in confinement. We attribute its origin, instead, to the combination of geometry, orientation, and specific composition of the surface in the two types of nanostructures: the uniform cation-terminated faces, which confer superior stability to tetrahedral NCs,[16] lead to a weaker hole confinement, compared to the cation-*rich* faceting in spherical structures. Indeed, as can clearly be seen from Figure 1, in tetrahedral NCs, each face is composed entirely of cations, whereas due to the nature of its faceting, the surface of spherical NCs exhibits a variety of facet sizes and orientations and mixed composition, even in the case of a nominally cation-rich surface. A consequence of the latter combination is a more effective hole confinement. We find that the deconfinement effect resulting from the large area, single-orientation, single-atomic-composition of the faces, peculiar to TNCs, increases with increasing hole effective mass. It follows that In-based materials are more affected than Cd-based ones and InP NCs more than other In-based ones, in agreement with recent findings,[24] where the optical properties of spherical NCs made of this material were found to be profoundly influenced by their surface composition, and where In-terminated surfaces were associated with large hole deconfinement effects. Interestingly, we find that, if the stoichiometry was reversed in the InP structures with a similar number of atoms considered above, (we note that this is a purely academic exercise, as, due to their growth process, tetrahedral NCs can currently be synthesized only with cation-terminated surfaces[10,16]), the hole confinement would be stronger in P-terminated tetrahedral NCs than in spherical NCs with P-rich surfaces, whereas the opposite would be true for the electron, which would experience a stronger confinement in spheres with P-rich surfaces. Figure S3 (Supporting Information) shows the energy difference $\Delta E_{shape}$ between the calculated CBM or VBM energies in the two shapes (with similar volume) as a function of the material for structures with both cation- (cat, squares) and


https://doi.org/10.1021/acs.chemmater.3c01643
Chem. Mater. 2024, 36, 1162−1171

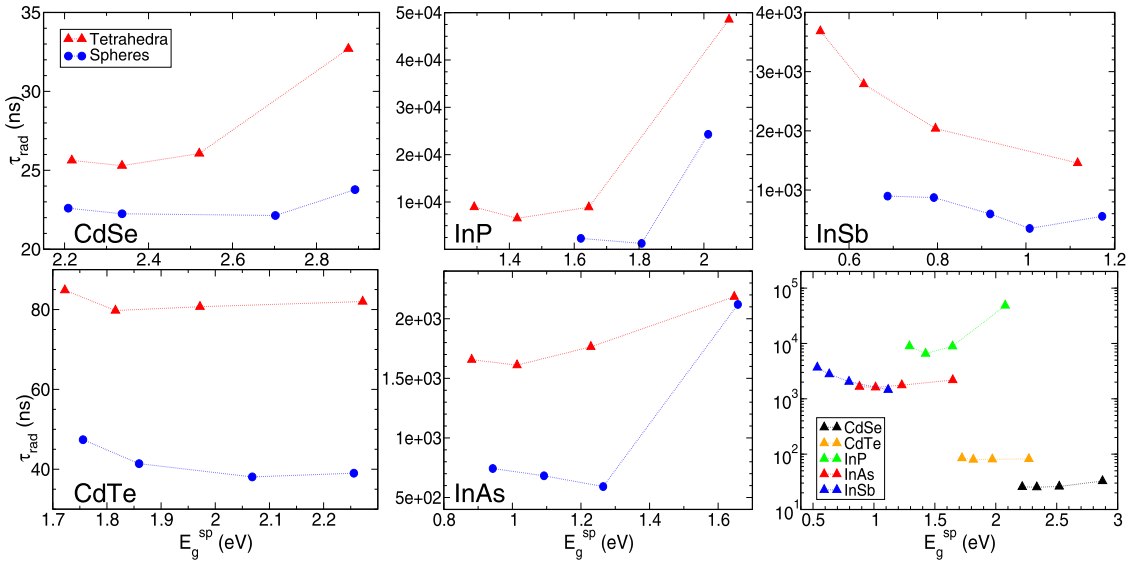


**Figure 4.** Radiative recombination times (in ns) as a function of the single-particle gap $E_g^{sp}$, calculated for tetrahedral (triangles) and spherical (circles) NCs of different II−VI and III−V materials. The dotted lines are a guide to the eye. All calculations are performed by assuming a refractive index of 1.497 (toluene) for the NC environment.

anion- (an, diamonds) terminated surfaces.[42] $\Delta E_{shape} = E_{sphere} - E_{tetrahedron}$ for the CBM and $\Delta E_{shape} = E_{tetrahedron} - E_{sphere}$ for the VBM, so that, for both band edges, positive [negative] values of $\Delta E_{shape}$ correspond to a stronger confinement in spherical [tetrahedral] NCs (yellow [orange] region in Figure S3, Supporting Information). We see that, for all materials, in cation-terminated structures, the hole (empty squares) is always more strongly confined in spherical NCs, whereas the opposite is true in anion-terminated NCs, where the hole (empty diamonds) experiences a stronger confinement in tetrahedral NCs in nearly all cases (in InSb and CdTe, the VBM position is very similar in spheres and tetrahedra).

In Figure S4 (Supporting Information) we show, instead, the energy difference $\Delta E_{term}$ between the electron (CBM) [hole (VBM)] band edge positions calculated, in the same structure (spheres, circles; tetrahedra, triangles), for different surface terminations, as a function of material. Here, $\Delta E_{term} = E_{cation} - E_{anion}$ for the CBM, and $\Delta E_{term} = E_{anion} - E_{cation}$ for the VBM, so that, for both band edges, positive [negative] values of $\Delta E_{term}$ correspond to a stronger confinement in cation-terminated [anion-terminated] NCs (yellow [orange] region in Figure S4, Supporting Information). We see that the VBM (empty symbols in Figure S4, Supporting Information) is always (i.e., in all materials and shapes considered) more strongly confined in structures with anion-terminated surfaces[42] (orange region in Figure S4, Supporting Information), whereas, in general, the opposite is true for the CBM (solid symbols in Figure S4, Supporting Information). Exceptions to this trend are found in Cd-based materials, where the CBM of tetrahedral NCs is more confined in anion-terminated structures. Furthermore, we find that in spherical NCs made of these materials, the confinement strength exhibited by both band edges is nearly independent of their surface composition.

We also find that the stoichiometry reversal, if possible to achieve experimentally, would be accompanied by a radical change in the k-space composition of both band edges in In-based tetrahedral NCs, where the Γ character of the CBM would decrease considerably in anion-terminated tetrahedra, accompanied by a large increase in the *L* component. Conversely, the Γ character of the VBM would be greater in anion-terminated tetrahedra than in cation-terminated ones, where the *L* component is more substantial. This may indicate that also the k-space composition of the CBM shown in Figure S2 (Supporting Information), that was suggested as the origin of the different degrees of localization in spherical and tetrahedral NCs exhibited in Figure 3, could be, in turn, a consequence of the surface termination. In contrast to this behavior, stoichiometry inversion has instead a much smaller effect (of the order of a few percent) on the k-space composition of spherical NCs (except for the case of InP, as previously found[24]) and of Cd-based tetrahedral NCs, which is however sufficient to cause the CBM localization in the latter for anion-terminated structures (Figure S3, Supporting Information).

Unfortunately, none of these effects can be captured by continuum-like (i.e., nonatomistic) approaches, such as the effective mass approximation[37] and the more sophisticated **k·p** method,[39] which are unable to differentiate between NCs with different stoichiometries or surface compositions.

Returning to the analysis of the properties of tetrahedral and spherical NCs with the same volume (Figures 2 and 3), however, we believe a more relevant comparison to be that between NCs with the same *confining size* (Figure 2, main panels), by which term we refer to the shortest dimension of the nanostructure (i.e., the diameter *d* and the height $h = \sqrt{2/3}\,L$, for the spherical and tetrahedral NCs, respectively). In terms of this parameter, Figure 2 shows confinement to be stronger in tetrahedra than in spheres for Cd-based NCs, whereas the opposite is true for In-based structures, again with a difference increasing from InAs, to InSb and to InP. The difference between the single-particle gaps of spheres and tetrahedra also exhibits a dependence on size in all materials: it increases with size for CdSe and InP, whereas it decreases with increasing size for all of the other materials. In other words, a tetrahedron and a sphere which exhibit very close $E_g^{sp}$ values also have nearly the same size if they are small Cd-based or large InAs NCs. In other materials, or for different sizes, their size may differ by as much as 2 nm (or even more if they are large and made of InP). This means that the shape of the NC may provide an additional degree of freedom to tailor its


https://doi.org/10.1021/acs.chemmater.3c01643
Chem. Mater. 2024, 36, 1162−1171

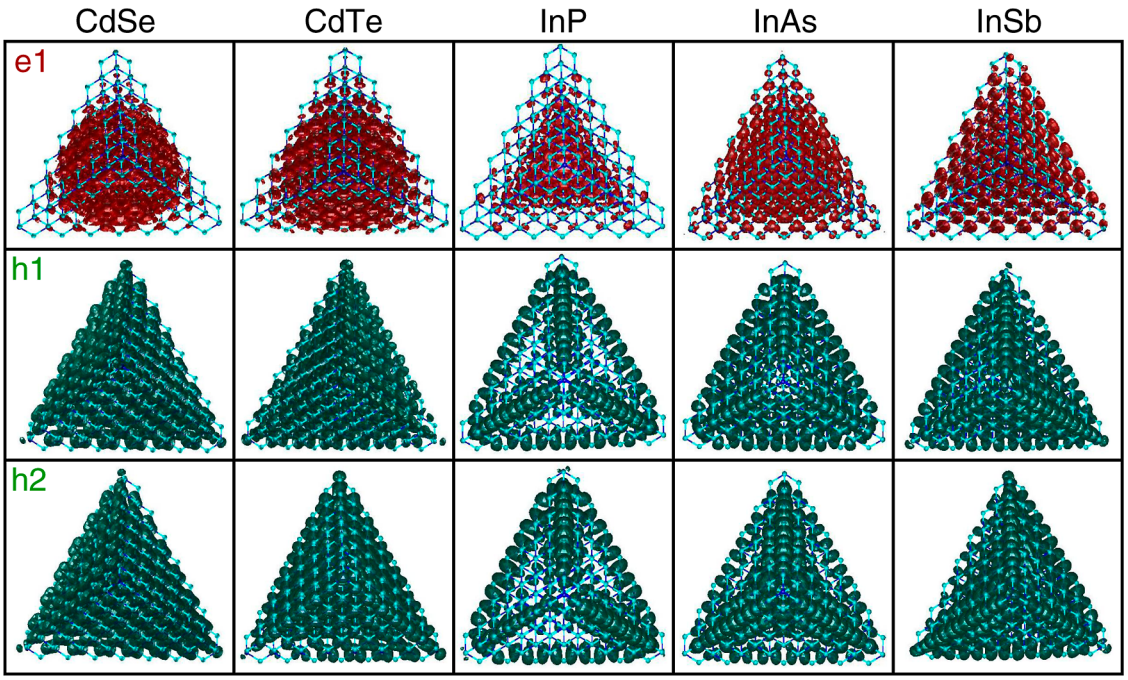


**Figure 5.** Top view of the charge density of the lowermost conduction ($e1$, CBM, red) and two uppermost valence band ($h1$ and $h2$, VBM, green) states, calculated for tetrahedral NCs with $L \sim 3$ nm made of different II−VI and III−V materials, superimposed onto the NC atomic structure. The blue and cyan spheres represent anions and cations, respectively.

volume-dependent properties, without altering its emission wavelength.

Among such properties are the (radiative and Auger) recombination lifetimes. We find (Figure 4) that the tetrahedral shape leads to a suppression of the radiative recombination, compared to spherical NCs with the same single-particle gap, whose magnitude depends on the specific material: it is smaller for Cd-based NCs (the ratio between lifetimes $\tau_R^{TNC}/\tau_R^{SNC}$ ranging from a factor of less than 1.3 for CdSe, to about 2 for CdTe) than for In-based ones ($2 \lesssim \tau_R^{TNC}/\tau_R^{SNC} \lesssim 3$ for InAs—except for the smallest dot—and InSb, and even larger for some InP NCs), again increasing with the material's hole effective mass.

A more conventional plot of the radiative recombination times as a function of size for both tetrahedral and spherical NCs is presented in Figure S5 (Supporting Information), where, to substantiate the accuracy of our calculations, we also include experimental data relative to spherical NCs.[43−51] All calculations are performed assuming a refractive index of 1.497 (toluene) for the NC environment to simulate NCs in solution.

In the case of InP, we find, in line with recent findings,[24] a strong dependence of the radiative times on the surface termination, leading to differences of up to 3 orders of magnitude between the exciton lifetimes calculated for spherical NCs with P- (patterned blue circles in Figure S5, Supporting Information) and In-rich surfaces (solid blue circles in Figure S5, Supporting Information). This is not the case for the other In-based NCs, where we found the radiative times of anion- and cation-rich surfaces to be of the same order of magnitude, with their difference decreasing with increasing radius.

To shed light on the origin of the trends exhibited by the radiative lifetimes, we display, in Figure 5, the band edges' charge distributions calculated for TNCs with $L \sim 3$ (Figure S6, Supporting Information, presents the same quantities for the corresponding spherical NCs with similar single-particle gaps). We find clear material-dependent differences: in CdSe, $e1$, the CBM, is nearly spherically symmetric, localizes in the tetrahedron core, and spills out onto the four facets' centers (evidenced, in Figure 5, by the red color covering the spheres representing the Cd and Se atoms), avoiding edges and corners; in CdTe, $e1$ looks very similar to CdSe, extending slightly more into the corners. These surprising results clearly indicate that the NC shape does not necessarily determine the symmetry of the electron wave functions, which may depend, instead, more critically on the NC composition.

The CBM's wave function spatial distribution in In-based TNCs is, instead, completely different: it has tetrahedral symmetry, and its localization depends on the specific anion, decreasing with the electron effective mass. The strong confinement to the NC core exhibited in InP becomes more relaxed in InAs and InSb, where $e1$ tends to occupy the whole NC volume. Similarly, the VBM charge density is localized prevalently in the NC interior and on one of the facets in Cd-based TNCs, whereas it is more on the edges (especially in InP), avoiding the corners (except in InSb), in In-based TNCs. The spatial charge distribution in spherical NCs exhibits a similar material dependence to that in TNCs (see Figure S6, Supporting Information). The behavior exhibited by the band edges in InP agrees with recent findings,[24] where, in spherical NCs, the presence of cation-rich surfaces was shown to lead to CBM wave functions well confined within the nanostructure core and to VBM charge densities more localized on the surface, with little density in the NC center. As a consequence, InP NCs of both shapes exhibit the smallest overlap between the band edge wave functions, as the CBM and VBM are localized in different spatial regions of the NC, hence they also display the longest radiative lifetimes. The comparison of the latter with experimentally measured exciton times of the order of tens of nanoseconds[49−51] (empty circles in Figure S5, Supporting Information) may therefore seem problematic. It needs to be noted, however, that


https://doi.org/10.1021/acs.chemmater.3c01643
Chem. Mater. 2024, 36, 1162−1171

experimental samples have a ZnX (X = Se, S) shell surrounding the InP core, whose growth crucially leads to a redshift of the excitonic energy. This shift was interpreted[50] as originating from a "spreading of the exciton wave functions into the shell". Based on the band edge alignments at the core/shell interface, it was then suggested[13] that in these heterostructures, "the electron may be less confined to the InP core".[13] This situation may indeed be similar to that simulated in our calculations for anion-terminated NCs (patterned blue circles, Figure S5, Supporting Information), where the electron wave function, although still confined to the core, exhibits some additional surface localization[24] (compared to cation-terminated InP NCs). In contrast, the hole is more confined to the core, leading to a larger overlap between their respective wave functions than in the case of cation-terminated NCs, resulting in a larger radiative rate, in good agreement with experiment.[49−51]

However, in general, it is difficult to rationalize the behavior of the calculated lifetimes, based uniquely on the graphical representation of the band edge wave functions. The gradual increase in the radiative times from CdSe to CdTe, to InAs, and finally to InSb can be explained in terms of the increase of the materials' dielectric constants and the concomitant decrease of their band gaps (see eq 3, Theoretical Method section) that would predict the 2 orders of magnitude difference between the radiative lifetimes in CdSe and InSb TNCs found here, assuming similar dipole matrix elements in both materials. The difference between tetrahedral and spherical structures is more complex to explain, considering that they are both made of the same material and that their single-particle gaps are similar. We find that, in general, the dipole matrix elements between the band edges are larger in spherical nanostructures than in tetrahedral nanostructures, leading to shorter radiative lifetimes in the former.

The opposite trend is found for the Auger recombination times (Figure 6), which we found to be slightly longer (although

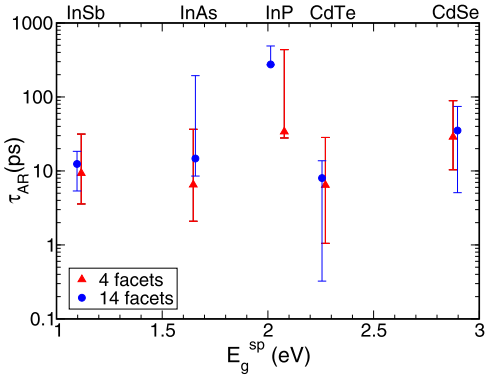


**Figure 6.** Auger recombination times as a function of single-particle gap, calculated for selected tetrahedral (4 facets, triangles) and nominally spherical but actually truncated octahedral (14 facets, circles) NCs of different II−VI and III−V materials. The error bars account for the effect of a size distribution of ±5% in the sample.

very similar, apart from InP nanostructures) in nominally spherical (but actually truncated octahedral) dots than in TNCs with nearly identical single-particle gaps. In InAs dots, a reduction in the number of facets from 14 (truncated octahedron) to 4 (tetrahedron) leads to an increase of AR rates by a factor of 2.26. This result is consistent with the behavior observed in $CsPbBr_3$ NCs,[20] where a similar increase in AR rates was associated with a 4.3-fold reduction in the number of NC facets. The fact that not in all cases displayed in Figure 6, the volume of the spherical NC is larger (albeit slightly) than that of the tetrahedral dot (for CdSe, the opposite is true; see Figure 2, insets), rules out the possibility that a volume scaling may be responsible for the difference in AR times. It is also interesting to note that the confinement, expressed in terms of the single-particle energy gap, is slightly stronger in the spherical NC in two (InAs and CdSe) out of five structures in Figure 6, seemingly ruling out a confinement-induced AR enhancement in TNCs. This conclusion, however, would be correct only if to larger values of $E_g^{sp}$ (which provide a measure of *exciton* confinement) also corresponded stronger confinement for both electrons and holes individually. Indeed, longer AR times were shown[52] to correlate with weaker *electron* confinement energies alone. We discussed earlier (Figure 3) that in structures with the same *volume*, the geometry that confines the electron more strongly depends on the specific material.

However, when we consider nanostructures with similar *emission energies*, we find (Figure 7) a strong correlation between

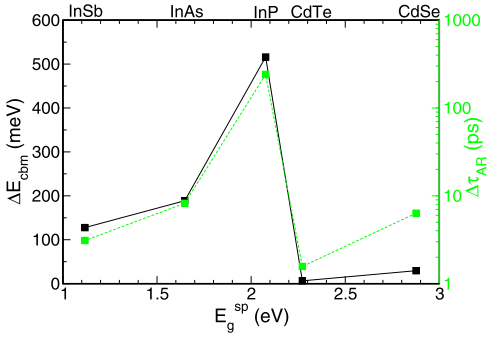


**Figure 7.** Difference in the calculated AR times of spherical and TNCs shown in Figure 6, $\Delta\tau_{AR} = \tau_{AR}^{SNC} - \tau_{AR}^{TNC}$, (right *y* axis and green solid squares, where a positive value indicates a faster AR in TNCs) and the difference in the position of the CBM in the two structures, $\Delta E_{cbm} = E_{cbm}^{TNC} - E_{cbm}^{SNC}$ (left *y* axis and solid black squares, where a positive value indicates a stronger confinement in TNCs), as a function of the single-particle energy gap.

the electron confinement energy (expressed in Figure 7 as the difference in the position of the CBM in the two structures, $\Delta E_{cbm} = E_{cbm}^{TNC} - E_{cbm}^{SNC}$, where a positive value indicates a stronger confinement in TNCs) and the speed of AR (expressed in Figure 7 as the difference in the respective AR times, $\Delta\tau_{AR} = \tau_{AR}^{SNC} - \tau_{AR}^{TNC}$, where a positive value indicates a faster AR in TNCs), showing that the origin of the faster Auger recombination we find in TNCs is indeed the stronger confinement experienced by the *electron* in these nanostructures.

Finally, in Figure 8, we present the calibration curves (i.e., the plots of the first exciton peak position vs size) for TNCs made of CdSe, CdTe, InP, InAs, and InSb, with side lengths ranging from $L \sim 2$ to $L \sim 8$ nm, including experimental data,[14,16,17,19,53] where available, for comparison and validation. Our theoretical predictions (solid triangles) are in excellent agreement with experiment (empty triangles) for all materials where measurements are available, confirming the accuracy of our calculations. In the case of InP TNCs, however, we note that the size of dots with a specific exciton peak position may vary by over 3 nm, when measured by different groups.[16,17,19]

Interestingly, it was found[19] that different choices of capping groups led to up to ∼71 meV (∼22 nm) shifts in the first absorption peak position in InP TNCs. In these materials, the


https://doi.org/10.1021/acs.chemmater.3c01643
Chem. Mater. 2024, 36, 1162−1171

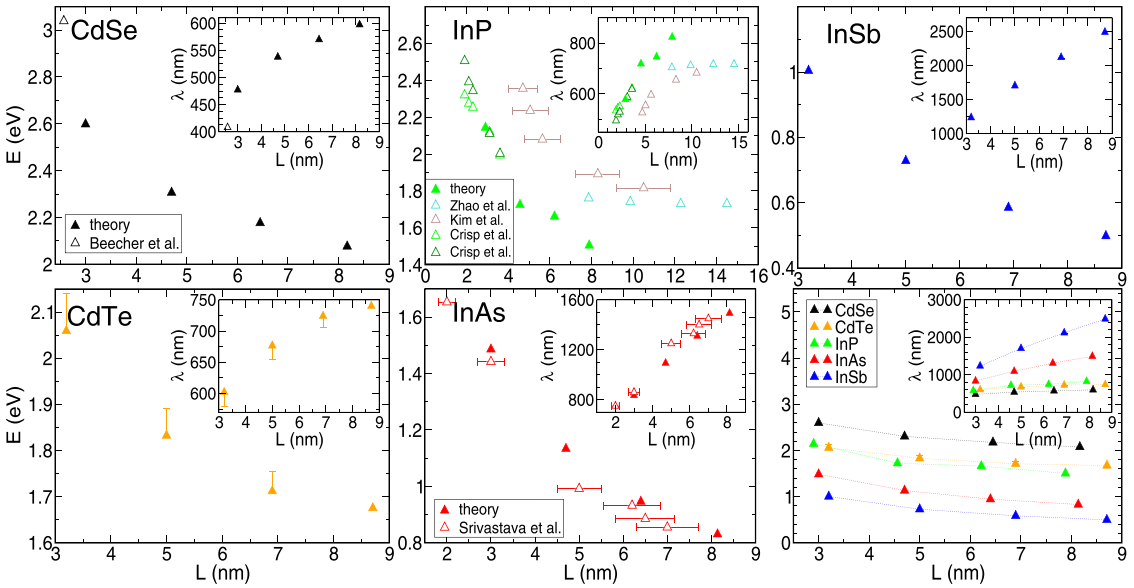


**Figure 8.** Absorption energy vs side length $L$ [where the energy is expressed both in electron volts—main panels—and in nanometers (insets)] calculated for tetrahedral NCs of different II−VI and III−V materials. Available experimental data[14,16,17,19,53] are also displayed for comparison. In the case of InP, the two sets of experimental data by Crisp et al.[19] refer to TNCs in a film (light green empty triangles) and in solution (dark green empty triangles). Reproduced from *Chem. Mater.* **2022**, 34, 8306−8315. Copyright 2022, American Chemical Society. Reproduced from *Angew. Chem. Int. Ed.* **2016**, 55, 3714−3718. Copyright 2016, Wiley-VCH. Reproduced from *ACS Appl. Energy Mater.* **2018**, 1, 6569−6576. Copyright 2018, American Chemical Society. Reproduced from *Chem. Mater.* **2016**, 28, 6797−6802. Copyright 2016, American Chemical Society.

same peak also exhibited redshifts of up to 186 meV (40 nm) when the NCs were transferred from the solution phase to a film. Given this high sensitivity exhibited by InP TNCs to the preparation conditions, therefore, the discrepancies between experimental measurements evidenced in Figure 8 may be due to different NC synthesis protocols and sample conditions.

## CONCLUSIONS

We provided a comprehensive theoretical characterization of tetrahedral NCs made of technologically relevant Cd-based and In-based materials, including much needed calibration curves, band edge positions, and the size dependence of radiative recombination times, for side lengths ranging from ∼3 to over 8 nm, corresponding to structures containing from about 300 to over 3300 atoms. Our results showed excellent agreement with the available experimental data. Side-by-side comparison was also presented with the properties of nominally spherical NCs made of the same materials, as a function of both volume and confinement size, highlighting differences and similarities between the two types of structures, which were analyzed and discussed in terms of shape, degree of confinement, and number of facets. We showed that simple single-band, effective-mass calculations are unsuitable to predict the correct confinement hierarchy in NCs with different shapes and the same volume. In this respect, we found that the optical properties of Cd-based tetrahedral and spherical dots with similar volumes are similar whereas those of In-based ones are not. A nontrivial interplay between geometry and composition of the surfaces in the two shapes, leading to different degrees of electron and hole confinement and of k-space composition of their wave functions, was suggested as the possible origin of such differences. We also found a material dependence in the band edges' charge densities localization, indicating that the symmetry of the confined electron wave function is not necessarily determined by the NC shape.

Our results provide compelling evidence for the need of accurate, bespoke calibration curves for TNCs, showing that, depending on their composition, a tetrahedron and a sphere that exhibit very close PL energies may differ in size by over 2 nm. This property can be exploited to tailor the volume-dependent properties of a nanostructure by shape engineering without altering its emission wavelength. In this respect, we found that both radiative and Auger recombination processes can be enhanced or suppressed, depending on the specific choice of NC shape. In general, our results show that spherical dots exhibit faster radiative and slower Auger recombination times, compared with TNC emitting at similar energies, making them a better choice for applications in lasers and light-emitting devices, whereas TNCs, with their higher mobilities and longer lifetimes, would be better suited for applications requiring fast carrier transport, such as in field-effect transistors and photovoltaic devices.

Comparing structures with similar confinement sizes (i.e., $d$ for spheres and $h = \sqrt{2/3}L$ for tetrahedra), Cd-based TNCs emit at higher (albeit slightly) energies than their spherical counterparts. The opposite is true in In-based nanostructures, where the PL of a spherical NC can be up to 0.5 eV higher in energy than that of a TNC with $h \approx d$. Furthermore, our results were broadly consistent with recent observations of an increase in AR rates with a reduction in the number of facets reported for $CsPbBr_3$ NCs. Our analysis, however, ruled out the volume scaling effect suggested in that case, as the origin of this behavior in TNCs, in favor of a confinement-induced AR enhancement, which correlates with the reduction of the number of facets. If supported by further experimental evidence, this result could open the way to AR engineering via facet design.


https://doi.org/10.1021/acs.chemmater.3c01643
Chem. Mater. 2024, 36, 1162−1171

## ■ ASSOCIATED CONTENT

### Supporting Information

The Supporting Information is available free of charge at https://pubs.acs.org/doi/10.1021/acs.chemmater.3c01643.

Band edges positions as a function of size; k-space composition of the CBM wave function in spherical and tetrahedral nanostructures; difference between the electron (CBM) [hole (VBM)] band edge positions $\Delta E_{shape}$ calculated in spherical and tetrahedral NCs as a function of material, for different surface terminations; difference between the electron (CBM) [hole (VBM)] band edge positions $\Delta E_{term}$ calculated, in the same structure, for different surface terminations as a function of material, for spherical and tetrahedral NCs; radiative recombination times; and band edge charge densities calculated for spherical nanostructures (PDF)

## ■ AUTHOR INFORMATION


### Corresponding Author

**Marco Califano** − *Pollard Institute, School of Electronic and Electrical Engineering, University of Leeds, Leeds LS2 9JT, U.K.; Bragg Centre for Materials Research University of Leeds, Leeds LS2 9JT, U.K.;* orcid.org/0000-0003-3199-3896; Email: m.califano@leeds.ac.uk

Complete contact information is available at: https://pubs.acs.org/10.1021/acs.chemmater.3c01643


### Notes

The author declares no competing financial interest.

## ■ ACKNOWLEDGMENTS

This work was undertaken on ARC3, part of the High-Performance Computing Facilities at the University of Leeds, UK. M.C. gratefully acknowledges financial support from the School of Electronic & Electrical Engineering, University of Leeds.

## ■ REFERENCES


(1) Rossetti, R.; Nakahara, S.; Brus, L. E. Quantum Size Effects in the Redox Potentials, Resonance Raman Spectra, and Electronic Spectra of CdS Crystallites in Aqueous Solution. *J. Chem. Phys.* **1983**, *79*, 1086−1088.

(2) Kovalenko, M. V.; Manna, L.; Cabot, A.; Hens, Z.; Talapin, D. V.; Kagan, C. R.; Klimov, V. I.; Rogach, A. L.; Reiss, P.; Milliron, D. J.; et al. Prospects of Nanoscience with Nanocrystals. *ACS Nano* **2015**, *9*, 1012−1057.

(3) Kagan, C. R.; Lifshitz, E.; Sargent, E. H.; Talapin, D. V. Building Devices from Colloidal Quantum Dots. *Science* **2016**, *353*, aac5523.

(4) *Quantum Dot Market by Material (Cadmium-based, Cadmium-Free), Product (Quantum Dot Displays, Other Products), Vertical (Consumer, Commercial, Healthcare, Defense, Telecommunications), and Geography (2021−2026)—Market Research Report*, 2023. https://www.marketsandmarkets.com/Market-Reports/quantum-dots-qd-market-694.html (accessed March 1, 2023).

(5) Manna, L.; Milliron, D. J.; Meisel, A.; Scher, E. C.; Alivisatos, A. P. Controlled Growth of Tetrapod-Branched Inorganic Nanocrystals. *Nat. Mater.* **2003**, *2*, 382−385.

(6) Deka, S.; Miszta, K.; Dorfs, D.; Genovese, A.; Bertoni, G.; Manna, L. Octapod-Shaped Colloidal Nanocrystals of Cadmium Chalcogenides via "One-Pot" Cation Exchange and Seeded Growth. *Nano Lett.* **2010**, *10*, 3770−3776.

(7) Arora, D.; Lian, J.; Xu, Y.; Wu, W. Y.; Chan, Y. T. Branched Heterostructured Semiconductor Nanocrystals with Various Branch Orders via a Facet-to-Facet Linking Process. *ACS Nano* **2020**, *14*, 10337−10345.

(8) Kanaras, A. G.; Sonnichsen, C.; Liu, H. T.; Alivisatos, A. P. Controlled Synthesis of Hyperbranched Inorganic Nanocrystals with Rich Three-Dimensional Structures. *Nano Lett.* **2005**, *5*, 2164−2167.

(9) Kwon, Y.; Bang, G.; Kim, J.; Agnes, A.; Kim, S. Synthesis of InP Branched Nanostructures by Controlling the Intermediate Nanoclusters. *J. Mater. Chem. C* **2020**, *8*, 1118−1124.

(10) Kim, Y.; Choi, H.; Lee, Y.; Koh, W.-k.; Cho, E.; Kim, T.; Kim, H.; Kim, Y. H.; Jeong, H. Y.; Jeong, S. Tailored Growth of Single-Crystalline InP Tetrapods. *Nat. Commun.* **2021**, *12*, 4454.

(11) Oron, D.; Kazes, M.; Banin, U. Multiexcitons in Type-II Colloidal Semiconductor Quantum Dots. *Phys. Rev. B* **2007**, *75*, 035330.

(12) Karel Čapek, R.; Moreels, I.; Lambert, K.; De Muynck, D.; Zhao, Q.; Van Tomme, A.; Vanhaecke, F.; Hens, Z. Optical Properties of Zincblende Cadmium Selenide Quantum Dots. *J. Phys. Chem. C* **2010**, *114*, 6371−6376.

(13) Tessier, M. D.; Dupont, D.; De Nolf, K.; De Roo, J.; Hens, Z. Economic and Size-Tunable Synthesis of InP/ZnE (E = S, Se) Colloidal Quantum Dots. *Chem. Mater.* **2015**, *27*, 4893−4898.

(14) Srivastava, V.; Janke, E. M.; Diroll, B. T.; Schaller, R. D.; Talapin, D. V. Facile, Economic and Size-Tunable Synthesis of Metal Arsenide Nanocrystals. *Chem. Mater.* **2016**, *28*, 6797−6802.

(15) Gupta, A.; Ondry, J. C.; Chen, M.; Hudson, M. H.; Coropceanu, I.; Sarma, N. A.; Talapin, D. V. Diffusion-Limited Kinetics of Isovalent Cation Exchange in III−V Nanocrystals Dispersed in Molten Salt Reaction Media. *Nano Lett.* **2022**, *22*, 6545−6552.

(16) Kim, K.; Yoo, D.; Choi, H.; Tamang, S.; Ko, J.-H.; Kim, S.; Kim, Y.-H.; Jeong, S. Halide-Amine Co-Passivated Indium Phosphide Colloidal Quantum Dots in Tetrahedral Shape. *Angew. Chem., Int. Ed.* **2016**, *55*, 3714−3718.

(17) Zhao, T.; Zhao, Q.; Lee, J.; Yang, S.; Wang, H.; Chuang, M.-Y.; He, Y.; Thompson, S. M.; Liu, G.; Oh, N.; Murray, C. B.; Kagan, C. R. Engineering the Surface Chemistry of Colloidal InP Quantum Dots for Charge Transport. *Chem. Mater.* **2022**, *34*, 8306−8315.

(18) Liu, W.; Lee, J.-S.; Talapin, D. V. III−V Nanocrystals Capped with Molecular Metal Chalcogenide Ligands: High Electron Mobility and Ambipolar Photoresponse. *J. Am. Chem. Soc.* **2013**, *135*, 1349−1357.

(19) Crisp, R. W.; Kirkwood, N.; Grimaldi, G.; Kinge, S.; Siebbeles, L. D. A.; Houtepen, A. J. Highly Photoconductive InP Quantum Dots Films and Solar Cells. *ACS Appl. Energy Mater.* **2018**, *1*, 6569−6576.

(20) Bera, S. K.; Bera, S.; Shrivastava, M.; Pradhan, N.; Adarsh, K. V. Facet Engineering for Amplified Spontaneous Emission in Metal Halide Perovskite Nanocrystals. *Nano Lett.* **2022**, *22*, 8908−8916.

(21) Robel, I.; Gresback, R.; Kortshagen, U.; Schaller, R. D.; Klimov, V. I. Universal Size-Dependent Trend in Auger Recombination in Direct-Gap and Indirect-Gap Semiconductor Nanocrystals. *Phys. Rev. Lett.* **2009**, *102*, 177404.

(22) Wang, L.-W.; Zunger, A. Local-Density-Derived Semiempirical Pseudopotentials. *Phys. Rev. B* **1995**, *51*, 17 398−17416.

(23) Sills, A.; Harrison, P.; Califano, M. Exciton Dynamics in InSb Colloidal Quantum Dots. *J. Phys. Chem. Lett.* **2016**, *7*, 31−35.

(24) Rodosthenous, P.; Gómez-Campos, F. M.; Califano, M. Tuning the Radiative Lifetime in InP Colloidal Quantum Dots by Controlling the Surface Stoichiometry. *J. Phys. Chem. Lett.* **2020**, *11*, 10124−10130.

(25) Graf, P. A.; Kim, K.; Jones, W. B.; Wang, L. W. Surface Passivation Optimization Using DIRECT. *J. Comput. Phys.* **2007**, *224*, 824−835.

(26) Franceschetti, A.; Fu, H.; Wang, L.-W.; Zunger, A. Many-body Pseudopotential Theory of Excitons in InP and CdSe Quantum Dots. *Phys. Rev. B* **1999**, *60*, 1819−1829.

(27) Aurenhammer, F. Voronoi Diagrams—A Survey of a Fundamental Geometric Data Structure. *ACM Comput. Surv.* **1991**, *23*, 345−405.

(28) Okabe, A.; Boots, B.; Sugihara, K.; Chiu, S. N. *Spatial Tessellations—Concepts and Applications of Voronoi Diagrams*, 2nd ed.; John Wiley, 2000, ISBN 0−471−98635−6.

(29) Jasieniak, J.; Califano, M.; Watkins, S. E. Size-Dependent Valence and Conduction Band-Edge Energies of Semiconductor Nanocrystals. *ACS Nano* **2011**, *5*, 5888−5902.
(30) Califano, M. Origins of Photoluminescence Decay Kinetics in CdTe Colloidal Quantum Dots. *ACS Nano* **2015**, *9*, 2960−2967.
(31) Wang, L.-W.; Califano, M.; Zunger, A.; Franceschetti, A. Pseudopotential Theory of Auger Processes in CdSe Quantum Dots. *Phys. Rev. Lett.* **2003**, *91*, 056404.
(32) Li, J.; Wang. Shape Effects on Electronic States of Nanocrystals. *Nano Lett.* **2003**, *3*, 1357−1363.
(33) Zhou, Y.; Califano, M. Decoupling Radiative and Auger Processes in Semiconductor Nanocrystals by Shape Engineering. *J. Phys. Chem. Lett.* **2021**, *12*, 9155−9161.
(34) Califano, M.; Zhou, Y. Inverse-Designed Semiconductor Nanocatalysts for Targeted $CO_2$ Reduction in Water. *Nanoscale* **2021**, *13*, 10024−10034.
(35) Dexter, D. L. *Solid State Physics*; Academic Press Inc.: New York, 1958; Vol. *6*, pp 358−361.
(36) Califano, M. Suppression of Auger Recombination in Nanocrystals via Ligand-Assisted Wave Function Engineering in Reciprocal Space. *J. Phys. Chem. Lett.* **2018**, *9*, 2098−2104.
(37) Li, W.-K.; Blinder, S. M. Variational Solution for Particle in a Regular Tetrahedron. *Chem. Phys. Lett.* **2010**, *496*, 339−340.
(38) $N_{atoms}$ provides a much more accurate estimate of the nanostructure's volume than any geometrical formula using approximated size measurements.
(39) Fu, H.; Wang, L.-W.; Zunger, A. Applicability of the **k·p** Method to the Electronic Structure of Quantum Dots. *Phys. Rev. B* **1998**, *57*, 9971−9987.
(40) Califano, M.; Lu, R.; Zhou, Y. Indirect to Direct Band Gap Transformation by Surface Engineering in Semiconductor Nanostructures. *ACS Nano* **2021**, *15*, 20181−20191.
(41) For each material, we compare NCs that have volumes as close as possible in Figure 3 i.e, for InSb we consider NCs with $N_{atoms} \sim 800$, for CdTe $N_{atoms} \sim 1800$ and for InP $N_{atoms} \sim 800$.
(42) In the case of spherical dots we refer to cation- or anion- rich surfaces due to the nature of their faceting.
(43) Gong, K.; Zeng, Y.; Kelley, D. F. Extinction Coefficients, Oscillator Strengths, and Radiative Lifetimes of CdSe, CdTe, and CdTe/CdSe Nanocrystals. *J. Phys. Chem. C* **2013**, *117*, 20268−20279.
(44) Schaller, R. D.; Pietryga, J. M.; Klimov, V. I. Carrier Multiplication in InAs Nanocrystal Quantum Dots with an Onset Defined by the Energy Conservation Limit. *Nano Lett.* **2007**, *7*, 3469−3476.
(45) Pijpers, J. J. H.; Hendry, E.; Milder, M. T. W.; Fanciulli, R.; Savolainen, J.; Herek, J. L.; Vanmaekelbergh, D.; Ruhman, S.; Mocatta, D.; Oron, D.; Aharoni, A.; Banin, U.; Bonn, M. Carrier Multiplication and Its Reduction by Photodoping in Colloidal InAs Quantum Dots. *J. Phys. Chem. C* **2007**, *111*, 4146−4152.
(46) Aharoni, A.; Oron, D.; Banin, U.; Rabani, E.; Jortner, J. Long-Range Electronic-to-Vibrational Energy Transfer from Nanocrystals to Their Surrounding Matrix Environment. *Phys. Rev. Lett.* **2008**, *100*, 057404.
(47) Busatto, S.; de Ruiter, M.; Jastrzebski, J. T. B. H.; Albrecht, W.; Pinchetti, V.; Brovelli, S.; Bals, S.; Moret, M.-E.; de Mello Donega, C. Luminescent Colloidal InSb Quantum Dots from In Situ Generated Single-Source Precursor. *ACS Nano* **2020**, *14*, 13146−13160.
(48) Liu, W.; Chang, A. Y.; Schaller, R. D.; Talapin, D. V. Colloidal InSb Nanocrystals. *J. Am. Chem. Soc.* **2012**, *134*, 20258−20261.
(49) Biadala, L.; Siebers, B.; Beyazit, Y.; Tessier, M. D.; Dupont, D.; Hens, Z.; Yakovlev, D. R.; Bayer, M. Band-Edge Exciton Fine Structure and Recombination Dynamics in InP/ZnS Colloidal Nanocrystals. *ACS Nano* **2016**, *10*, 3356−3364.
(50) Li, Y.; Hou, X.; Dai, X.; Yao, Z.; Lv, L.; Jin, Y.; Peng, X. Stoichiometry-Controlled InP-Based Quantum Dots: Synthesis, Photoluminescence, and Electroluminescence. *J. Am. Chem. Soc.* **2019**, *141*, 6448−6452.
(51) Chandrasekaran, V.; Tessier, M. D.; Dupont, D.; Geiregat, P.; Hens, Z.; Brainis, E. Nearly Blinking-Free, High-Purity Single-Photon Emission by Colloidal InP/ZnSe Quantum Dots. *Nano Lett.* **2017**, *17*, 6104−6109.
(52) Melnychuk, C.; Guyot-Sionnest, P. Multicarrier Dynamics in Quantum Dots. *Chem. Rev.* **2021**, *121*, 2325−2372.
(53) Beecher, A. N.; Yang, X.; Palmer, J. H.; LaGrassa, A. L.; Juhas, P.; Billinge, S. J.; Owen, J. S. Atomic Structures and Gram Scale Synthesis of Three Tetrahedral Quantum Dots. *J. Am. Chem. Soc.* **2014**, *136*, 10645−10653.


https://doi.org/10.1021/acs.chemmater.3c01643
*Chem. Mater.* 2024, 36, 1162−1171